

**Impact on porous targets: Penetration, crater formation, target compaction, and ejection**Christian Ringl,<sup>1</sup> Eduardo M. Bringa,<sup>2</sup> and Herbert M. Urbassek<sup>1,\*</sup><sup>1</sup>*Fachbereich Physik und Forschungszentrum OPTIMAS, Universität Kaiserslautern, Erwin-Schrödinger-Straße, D-67663 Kaiserslautern, Germany*<sup>2</sup>*CONICET and Instituto de Ciencias Básicas, Universidad Nacional de Cuyo, Mendoza, 5500 Argentina*

(Received 3 July 2012; published 19 December 2012)

Using a granular-mechanics code, we study the impact of a sphere into a porous adhesive granular target, consisting of monodisperse silica grains. The model includes elastic repulsive, adhesive, and dissipative forces, as well as sliding, rolling, and twisting friction. Impact velocities of up to 30 m/s and target filling factors (densities) between 19% and 35% have been systematically studied. We find that the projectile is stopped by an effective drag force which is proportional to the square of its velocity. Target adhesion influences projectile stopping only below a critical velocity, which increases with adhesion. The penetration depth depends approximately logarithmically on the impact velocity and is inversely proportional to the target density. The excavated crater is of conical form and is surrounded by a compaction zone whose width increases but whose maximum value decreases with increasing target density. Grain ejection increases in proportion with impactor velocity. Grains are ejected which have originally been buried to a depth of  $8R_{\text{grain}}$  below the surface; the angular distribution favors oblique ejection with a maximum around  $45^\circ$ . The velocity distribution of ejected grains features a broad low-velocity maximum around 0.5–1 m/s but exhibits a high-velocity tail up to  $\sim 15\%$  of the projectile impact velocity.

DOI: [10.1103/PhysRevE.86.061313](https://doi.org/10.1103/PhysRevE.86.061313)

PACS number(s): 81.05.Rm, 79.20.Ap, 96.25.Pq, 95.30.Wi

**I. INTRODUCTION**

Impact into granular material has been studied intensely in the recent past, with particular emphasis on non-cohesive targets, such as dry sands [1–8]. Impacts into adhesive materials appears to have received less attention. However, such impacts are of prime importance in the field of planetary sciences. As an example, the mechanical properties of surfaces of planets, moons, asteroids, etc. can be determined from the dynamic behavior of impacting projectiles [9]. As one outstanding example, we mention the space mission DEEP IMPACT, in which an impactor (364 kg, 49% Cu) impinged with a velocity of 10.3 km/s on the comet Tempel 1 [10]. This comet is highly porous with a filling factor of around 30%–50% [11]. The objective of this mission was to learn about the structure of the comet nucleus by an analysis of the crater formed and of the ejecta. Similar impacts would occur (naturally) if compact objects like meteorites collide with comets, the surface of ice-covered moons, or planetary rings. As a final related example, one could consider the impacts of cometary material into the capture foam in the STARDUST mission [12], which have been extensively analyzed by continuum modeling of impact in low-density materials [13,14]. Such continuum modeling might become problematic as the size of the aggregates reaches micrometer-size scales.

The role of adhesive forces on the dynamics of granular matter has recently been nicely documented in an experimental study on the clustering of silica grains in granular streams [15]. This study revealed both the relevance of van der Waals adhesion forces on low-velocity dynamics and showed that rough grains will exhibit less cohesion than smooth grains.

Recent experiments have also demonstrated that interstitial gas contained in a granular target will affect the slowing-down

forces on the projectile, and hence the crater shape [16,17]. A high gas content induces the granular material to respond in a nearly incompressible, fluidlike manner, while in the absence of gas the target is able to compact more strongly, increasing energy dissipation and projectile deceleration. In the present context of astro-physical applications, however, we may safely assume that the gas content of our targets is near zero.

From a theoretical point of view, the modeling of such impacts is not trivial. Available granular-mechanics codes often favor nonadhesive grains since they care for larger grain sizes where adhesive forces may be neglected. The important work by Paszun and Dominik [18] and Wada *et al.* [19–23]—which aim at modeling porous adhesive material for the astrophysical and planetary context—has allowed up to now only the simulation of targets containing  $< 10,000$  grains, which is hardly sufficient for the modeling of impacts on extended targets. Finally, the established method of “smoothed particle hydrodynamics” (SPH)—which has proven successful for describing impacts on large bodies such as planets or moons [24]—needs to be carefully adjusted to include an appropriate porosity model [25–27], and might also fail in the micrometer-size scales needed for some astrophysics scenarios.

In the present paper, we use a recently developed code [28] for adhesive granular mechanics to investigate the problem of impact of a rigid sphere into a porous medium composed of adhesive grains. The projectile is 3 times larger than the grains of which the target is composed; this size has been chosen as a compromise between clarity of the results and computational effort (size of the simulation volume). While it would be interesting to use larger projectiles—to come closer to practical applications and also to vary projectile size and mass and study their influence—the present work concentrates on a fixed projectile size and studies the impact-induced processes in detail for this prototypical example.

\*urbassek@rhrk.uni-kl.de; <http://www.physik.uni-kl.de/urbassek/>

We focus on grains composed of monodisperse micrometer-sized silica spheres. By systematically varying the impact speed and the target porosity, we are able to characterize the effective force with which the projectile is slowed down, the dependence of the penetration on the target porosity, the crater size and shape, and the amount and characteristics of ejected material. Where data or theoretical analyses are available, we compare our results to those for nonadhesive granular targets.

## II. METHOD

### A. Granular mechanics algorithm

The details of our simulation method and granular-mechanics code have recently been published [28] and employed to simulate collisions of porous clusters [29]. In the following we only briefly describe the main features of our method.

Our porous targets consist of a collection of spherical grains, cf. Fig. 1. All of them possess the same properties (radius  $R_{\text{grain}}$ , elastic moduli, etc.). The grains only interact if the distance of their centers  $d < 2R_{\text{grain}}$ . As common in granular mechanics, the length  $\delta = 2R_{\text{grain}} - d$  is called the grain *overlap*, and interactions are nonzero only for  $\delta > 0$ .

Forces between grains are classified as *normal* and *tangential forces*. The normal force consists of a repulsive and an adhesive contribution. The repulsive part [30],

$$f_{\text{rep}} = \max \left\{ 0, \frac{4}{3} M \sqrt{R_{\text{red}}} \delta (\delta + A v_n) \right\}, \quad (1)$$

consists of a Hertzian  $\delta^{3/2}$  contribution, based on elastic theory, and a dissipative part, describing a viscoelastic contact [31]. Here  $R_{\text{red}} = R_{\text{grain}}/2$  is the reduced radius,  $M = Y/2(1 - \nu^2)$  is the reduced modulus,  $Y$  Young's modulus,  $\nu$  Poisson's ratio,  $v_n$  is the velocity component in normal direction, and  $A$  is an empirical factor modeling dissipation. The max operator in Eq. (1) prevents the force from becoming attractive when the two grains move away from each other with high velocity.

The adhesive part of the normal force is taken to be identical to the pull-off force needed to break a contact. According to

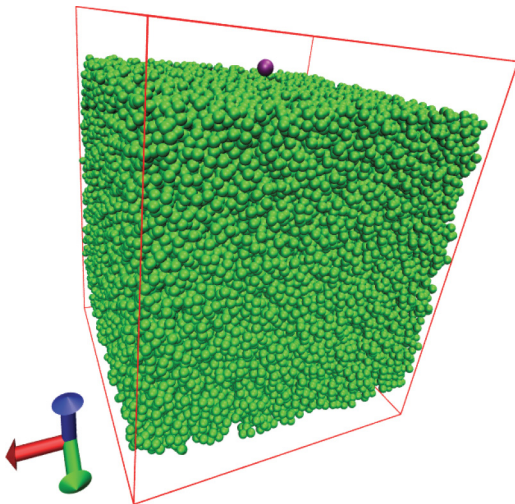


FIG. 1. (Color online) Target used for impact simulation, filling factor  $\phi = 26.7\%$ . Red: impacting sphere.

the widely used Derjaguin-Muller-Toporov model [32] it is given by

$$f_{\text{adh}} = 4\pi R_{\text{red}} \gamma. \quad (2)$$

Adhesion is characterized by the material-dependent parameter  $\gamma$ ; in our case, where grains consist of the same material,  $\gamma$  is twice the specific surface energy of the material.

Note that existing contact models [33–36] predict the adhesive force to follow a complex dependence on the distance between two grains, which we simplify by the constant value, Eq. (2) [28].

The tangential forces consist of several friction forces. Gliding friction,

$$f_{\text{slide}} = \frac{1}{2} G \pi a^2, \quad (3)$$

depends on the shear modulus  $G$  and the radius  $a = \sqrt{\delta R_{\text{red}}}$  of the contact area [37]. Rolling motion is decelerated by a torque [38],

$$D_r = 2 f_{\text{adh}} \xi_{\text{yield}}. \quad (4)$$

Here,  $\xi_{\text{yield}}$  is the distance which two grains can roll over each other without breaking their atomic contacts. Finally, also torsional motion is decelerated by a torque, whose strength is given by [38]

$$D_t = \frac{1}{3} G \frac{a^3}{\pi}. \quad (5)$$

In the actual implementation, we supplement the velocity independent friction force, Eq. (3), with a velocity proportional contribution (a viscous term), valid for small velocities. This has the effect that the abrupt jump in the sliding force, which occurs when the tangential velocity approaches zero, is smoothed. As a consequence, the grain contact is stabilized. For the other friction forces we proceed analogously. For details see Ref. [28].

The adhesive properties of our granular material are summarized in the surface energy  $\gamma$ . We note that this parameter also describes the energy needed to break the contact between two spheres; it is given by [28,29]

$$E_{\text{break}} = f_{\text{adh}} \delta_{\text{equ}}. \quad (6)$$

Here  $\delta_{\text{equ}}$  denotes the equilibrium distance between two grains in contact. It can be calculated from the requirement that at this distance  $f_{\text{rep}} = f_{\text{adh}}$ :

$$\delta_{\text{equ}} = \left( \frac{9\pi^2 \gamma^2 R_{\text{red}}}{M^2} \right)^{1/3}. \quad (7)$$

Thus the potential energy of a contact scales with the surface energy as  $E_{\text{break}} \propto \gamma^{5/3}$ .

Our simulations have been performed with the well-documented molecular-dynamics package LAMMPS [39] after the above features have been coded into this software.

### B. Parameter selection

The materials parameters are chosen as appropriate for  $\text{SiO}_2$  [40]: Young's modulus  $Y = 54$  GPa, Poisson's ratio  $\nu = 0.17$ , shear modulus  $G = Y/[2(1 + \nu)]$ , and  $\gamma = 0.05$  J  $\text{m}^{-2}$  is twice the specific surface energy of  $\text{SiO}_2$ .

The grain radius was kept fixed as  $R_{\text{grain}} = 0.76 \mu\text{m}$ . The density of the  $\text{SiO}_2$  grains amounts to  $\rho = 2 \times 10^3 \text{ kg m}^{-3}$  [41]. The mass of a grain amounts to  $m = 3.68 \times 10^{-15} \text{ kg}$ .

### C. System and simulation

The global filling factor of an ensemble of  $N$  grains—each with a volume  $V_{\text{grain}} = 4\pi R_{\text{grain}}^3/3$ —in a volume  $V$  is defined as  $\phi = NV_{\text{grain}}/V$ . We build porous targets with a specified filling factor as follows:

- (1) Set a grain at an arbitrary position in the volume.
- (2) Calculate the local filling factor for each grain; this is done by counting the number of grains in a sphere of radius  $5R_{\text{grain}}$  around it.
- (3) Determine the grain with the smallest local filling factor.
- (4) Attach a grain to it in random direction.
- (5) If the actual number of grains  $< N$ , go to step 2.

This simple algorithm distributes the grains homogeneously in the volume. We construct targets with filling factors between around 20% and 35%; the actual values were 19.1%, 22.8%, 26.7%, 30.7%, and 34.7%. The volume  $V$  was cubic with a side length of  $93R_{\text{grain}} = 70.7 \mu\text{m}$ . The maximum number of grains used, in the densest target, amounted to  $N = 70,000$ . The top and bottom surfaces of the target are free; at the sides we employ periodic boundary conditions.

As a projectile we employ a sphere with radius  $3R_{\text{grain}}$  and mass  $m_{\text{proj}} = 27m$ . Its elastic and contact properties are again those of silica. It does not possess any internal structure.

## III. RESULTS

### A. Stopping and penetration

When the projectile penetrates into the target, it feels an effective stopping force which results from its interaction with the grains and of the grains with each other. This stopping force  $F$  is *a priori* unknown. Let us assume it has a power-law dependence on the projectile velocity  $v$  with exponent  $\alpha$ ,

$$F = -f|v|^\alpha. \quad (8)$$

Such a law (with  $\alpha > 1$ ) leads to a decrease of the projectile velocity with time  $t$  as

$$t = \frac{m_{\text{proj}}}{f} \frac{1}{\alpha - 1} \left( \frac{1}{v^{\alpha-1}} - \frac{1}{v_0^{\alpha-1}} \right). \quad (9)$$

We tested our slowing-down data  $v(t)$  with such a law and conclude that our results are compatible with  $\alpha = 2$ ; a representative case is shown in Fig. 2. At later times than those shown in Fig. 2, the stopping law changes due to adhesion, cf. the Appendix Sec. A.

While for  $\alpha < 2$ , a power-law stopping force leads to finite penetration depths, they become (formally) infinite for  $\alpha \geq 2$ . Assuming particles to have stopped if they reach a threshold velocity  $v_{\text{th}}$  (threshold energy  $E_{\text{th}}$ ), we obtain for our case  $\alpha = 2$  a penetration depth of

$$D = \frac{m_{\text{proj}}}{f} \ln \frac{v_0}{v_{\text{th}}} \propto \ln \frac{E_0}{E_{\text{th}}}. \quad (10)$$

In this simple model it is assumed that the projectile follows a straight path while slowing down. Figure 3 assembles all our data and shows that such a logarithmic dependence appears

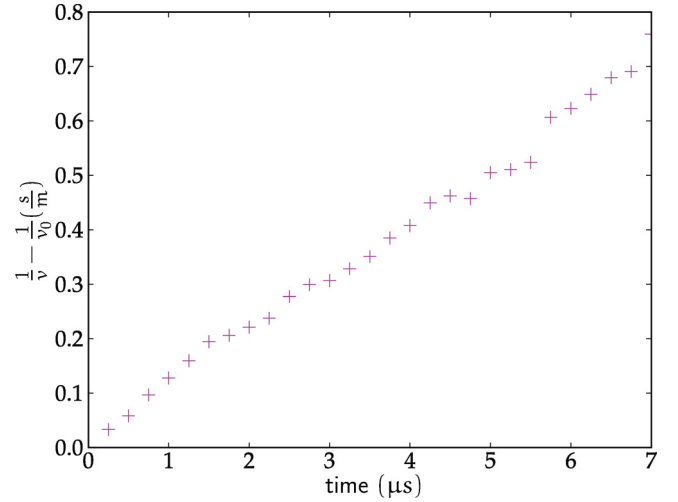


FIG. 2. (Color online) Slowing down of projectile (impact velocity 30 m/s) in a target (filling factor  $\phi = 30.7\%$ ). The linear dependence of  $(1/v - 1/v_0)$  on time  $t$ , cf. Eq. (9), is characteristic of a quadratic stopping force law, see text.

to be reasonably well fulfilled. In the simulation we assume the projectile to be stopped when its energy is below  $E_{\text{th}} = 1.0 \times 10^{-16} \text{ J}$ , corresponding to a velocity of  $v_{\text{th}} = 0.04 \text{ m/s}$ . We conclude from Fig. 3 that the penetration depth increases roughly logarithmically with impact energy; naturally more porous targets possess higher penetration depths.

The problem of penetration of impactors into granular media has been intensely studied in the recent past. Katsuragi and Durian [7], extending simulation studies by Tsimring and Volfson [6], recently proposed a “unified law” for penetration into granular material. They find that gravity leads to a depth-dependent contribution to the effective force acting on the projectile in the target, caused by the difference of the hydrostatic pressure on the upper and lower side of the impactor; this force is of course missing in our context. In addition, they find a drag force which is proportional to  $v^2$ , just as in our simulations. Such a drag force, caused by dynamic friction, has already been assumed in early studies

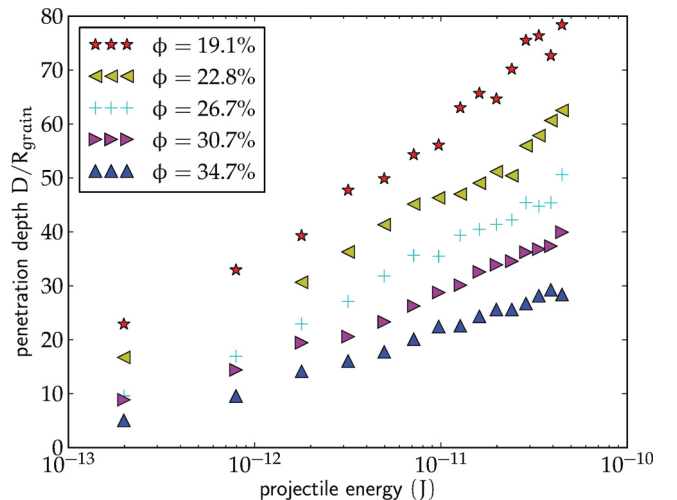


FIG. 3. (Color online) Dependence of penetration depth  $D$  on impact velocity  $v$  for various target filling factors  $\phi$ .

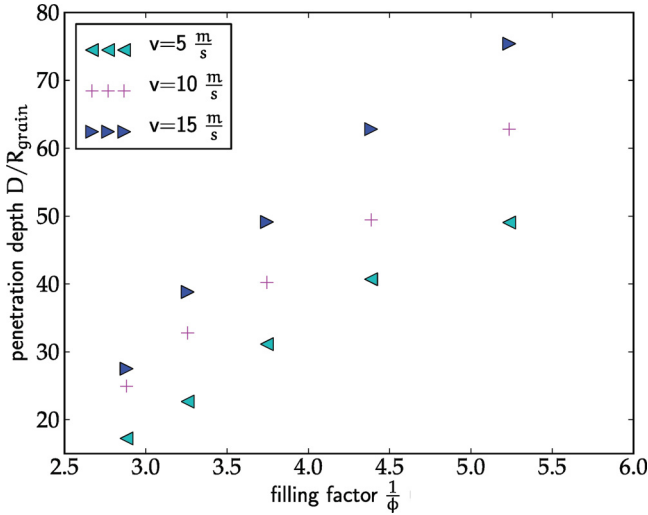


FIG. 4. (Color online) Dependence of penetration depth  $D$  on target filling factor  $\phi$  for various impact velocities  $v$ .

of high-speed ballistics, known as the Poncelet force law, cf., e.g., Ref. [42]. Granular material packed at low densities is a particular case of a highly porous material. Penetration of projectiles in highly porous media has been considered in a number of models, e.g., in Refs. [13] and [14].

We thus conclude that we find that Poncelet's law also describes the slowing down of projectiles in adhesive granular materials. Deviations from this conclusion occur at low impactor velocities and are described in the Appendix, Sec. A.

In Fig. 4 we display the dependence of the penetration depth on the target filling factor. In good approximation, an inverse relationship

$$D \propto \frac{1}{\phi} \quad (11)$$

can be observed, i.e., the penetration depth scales with the effective target density.

### B. Crater

During impact, the projectile digs a crater into the target, with a depth equal to the penetration depth. Figure 5 shows two exemplary cases. We note that the crater shape in this figure is similar to the shape of some of the craters shown in Ref. [13] for STARDUST craters. This suggests that some of our conclusions might still remain qualitatively valid at much larger impact energies, where the approximation of elastic granular material is no longer valid.

In Fig. 6(a) we display how the upper crater diameter evolves with impact speed. After an early increase for small velocities, the diameter saturates for velocities  $\gtrsim 20$  m/s at values of  $(20 - 30)R_{\text{grain}}$ ; this corresponds to 3–5 times the projectile diameter. Note that since the projectile penetration depth—and hence the crater depth—keeps increasing with velocity (cf. Fig. 3), the crater aspect ratio keeps increasing; for higher impact speeds, craters become increasingly tubelike.

The crater diameter decreases with target density  $\phi$ , cf. Fig. 6(b). We note that the decrease does not scale with  $1/\phi$ , in contrast to the penetration depth [Eq. (10), cf. Fig. 4]. This means that crater forms are not self-similar for materials with

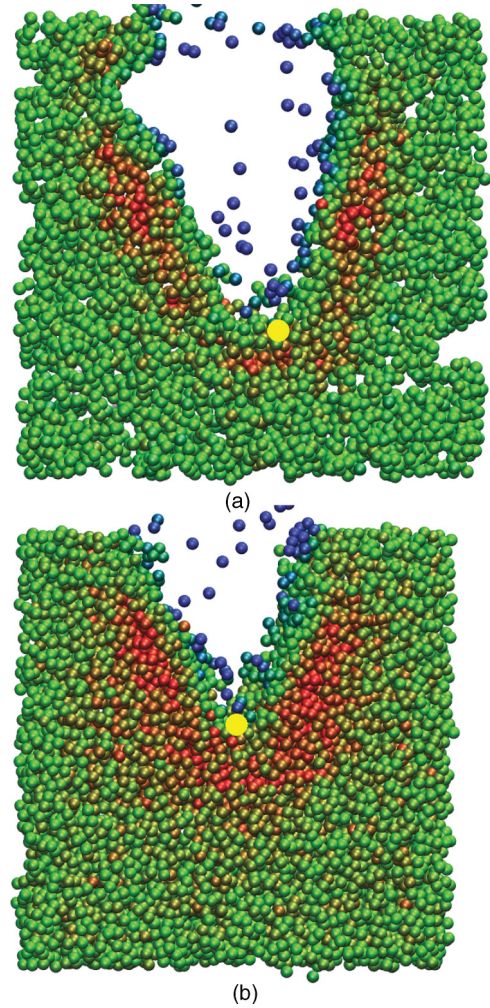


FIG. 5. (Color online) Craters caused by the impact of a projectile with velocity of 20 m/s into a target with filling factor of (a)  $\phi = 19.1\%$  and (b)  $\phi = 26.7\%$ . Color code denotes relative target compaction. Blue (red): 10% smaller (larger) filling factor than original target; green: original filling factor. The yellow sphere marks the position of the stopped projectile.

different porosities. The dependence of the crater aspect ratio on target density is summarized in Fig. 6(c). The highest aspect ratios are obtained in the most porous targets; here tubelike or conical impact craters with an aspect ratio of 2.5 are formed at the highest velocities investigated here. For denser targets, craters become increasingly hemispherical with an aspect ratio approaching 1.

### C. Target compaction

In Fig. 5, the region in the target which has been compacted by the impact has been highlighted. The features displayed for the two cases are observed quite generally in our simulations. The regions below and at the sides of the craters are found compacted; at the crater wall itself and towards the surface, we find only little target modification (besides an obvious target thinning immediately at the crater wall). The compacted region has a quite uniform thickness below and sideways to the crater.

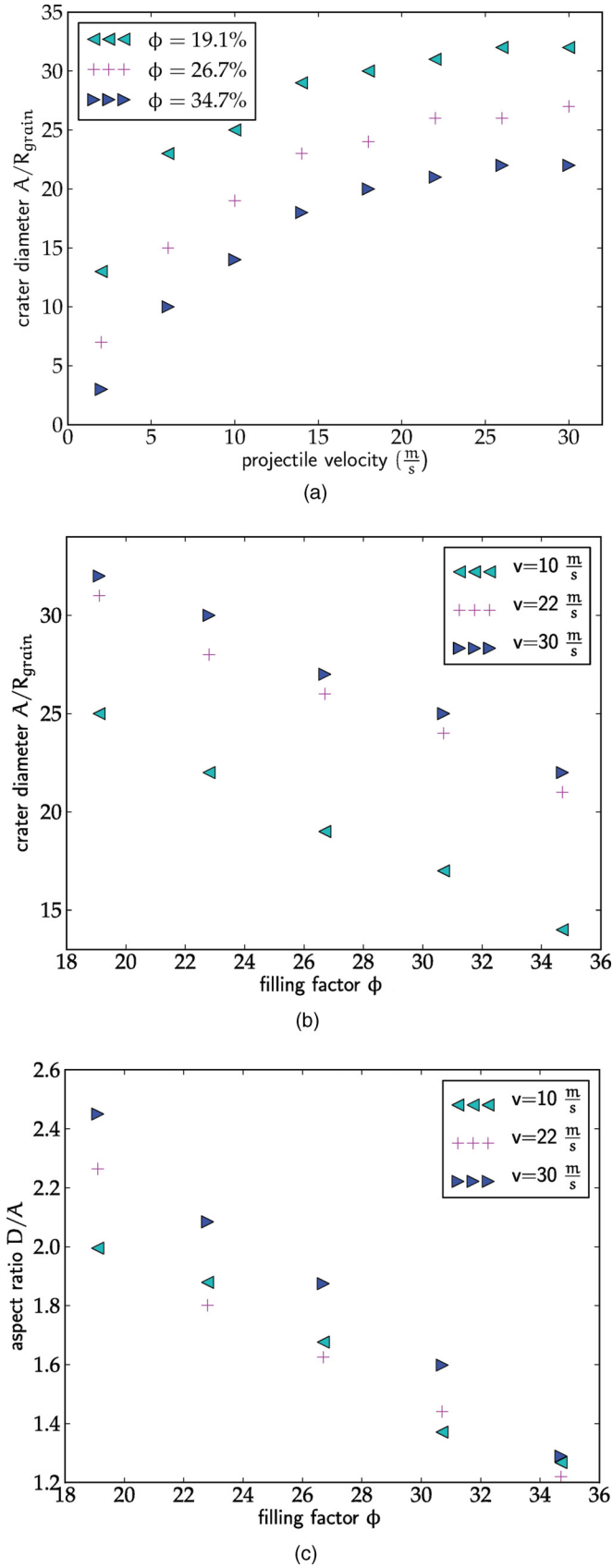


FIG. 6. (Color online) Dependence of the upper crater diameter on (a) impact speed and (b) filling factor. (c) Dependence of the crater aspect ratio on filling factor.

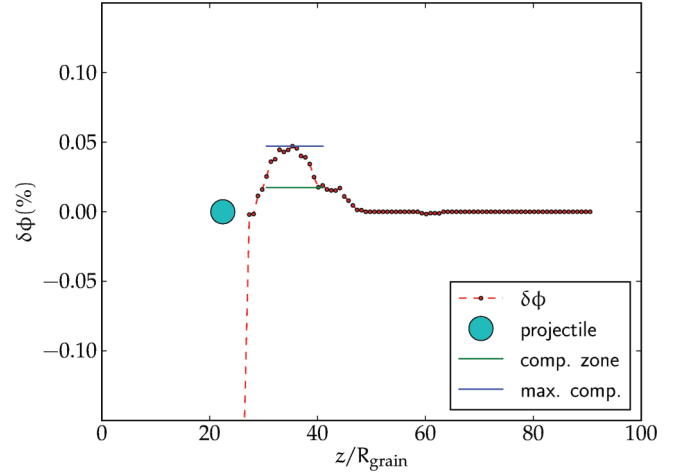


FIG. 7. (Color online) Change of local target filling factor  $\delta\phi$  with depth  $z$  into the target for impact of a projectile with velocity of 6 m/s into a target with filling factor of  $\phi = 26.7\%$ . The final position of the impactor is marked. The maximum compaction  $\delta\phi_{\max}$  and the width of the compacted zone  $w_{\text{mod}}$ —taken as the region where the change of the filling factor amounts to at least  $1/e = 37\%$  of  $\delta\phi_{\max}$ —are indicated.

In order to study this behavior quantitatively, we measure the local filling factor in a cylinder below the projectile impact point with a diameter equal to the projectile diameter and display the result for a representative example in Fig. 7; the position of the stopped projectile is also indicated. The modified target region is clearly defined. We denote the maximum change of the filling factor by  $\delta\phi_{\max}$ ; in addition, the width of the modified zone  $w_{\text{mod}}$  is taken as the region where the change of the filling factor amounts to at least  $1/e = 37\%$  of  $\delta\phi_{\max}$ .

Figure 8 shows the systematics of our results. Initially highly porous targets show a larger maximum compaction than initially dense targets. Even more pronounced is the dependence of the width of the compacted region, which increases significantly with the initial target filling factor. The dependence of both quantities on projectile speed is only mild and does not appear to be statistically significant.

#### D. Grain ejection

Projectile impact not only digs a crater into the target, but also ejects grains from it. This process is analogous to the sputtering known from ion impact into (nongranular) solids [43]. The number of grains ejected by the impact is called the ejection yield  $Y$ .

A grain was considered ejected when its height is above the original target surface and its velocity is above zero. Thus grains forming the crater rim [cf. Fig. 5(a)] are not counted as ejected, since they have vanishing velocity. On the other hand, a few low-energy grains are still moving in the otherwise empty crater volume and some of them may finally be ejected.

In Fig. 9, we display the ejection yield as a function of projectile velocity for a target of medium porosity. An approximately linear dependence of the ejection yield  $Y$  on projectile velocity  $v$ ,

$$Y = \alpha v, \tag{12}$$

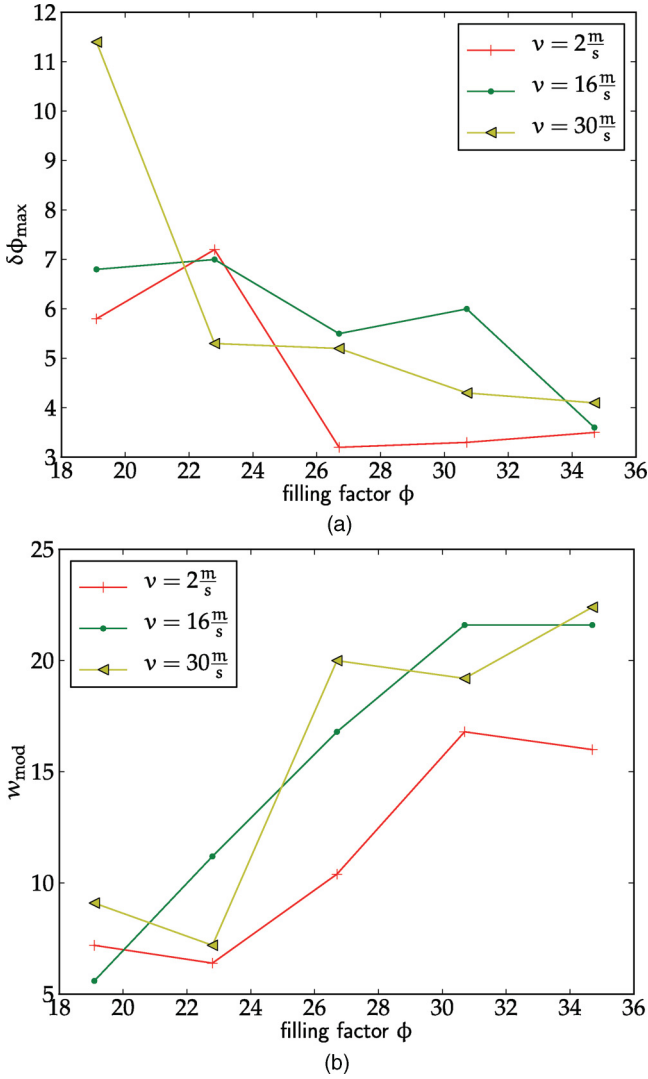


FIG. 8. (Color online) Dependence of the (a) maximum compaction and (b) width of the compacted zone on filling factor  $\phi$  for various impact velocities  $v$ .

is observed. This also happens in the other targets not shown here, with the exception of the smallest filling factor,  $\phi = 19.1\%$ , where fluctuations are largest. The proportionality constant  $\alpha$  in Eq. (12) assumes values of 1.05, 3.24, 3.46, 2.05, and 2.91 s/m with increasing filling factor. It thus appears that ejection is maximum for intermediate filling factors, but this conclusion is at the limit of the statistical relevance of our data.

In order to gain more insight into the ejection process, we analyze a particularly abundant case in more detail. We selected the case of intermediate filling factor and high velocity,  $\phi = 26.7\%$  and  $v = 30 \text{ m/s}$ , and simulated nine impact events; the impact point was varied randomly within a distance of  $3R_{\text{grain}}$ . We analyzed the ejection velocity  $v$ , the depth of origin  $z$  of the ejected grains, and the ejection angle  $\vartheta$  measured with respect to the surface normal. The results are plotted in Fig. 10.

Ejection energies have a broad maximum at around  $0.8 \times 10^{-15} \text{ J}$ , corresponding to velocities around  $0.5 \text{ m/s}$ . A fit of this distribution to a Maxwellian emission distribution (not shown) gives unphysically high ejection “temperatures” of

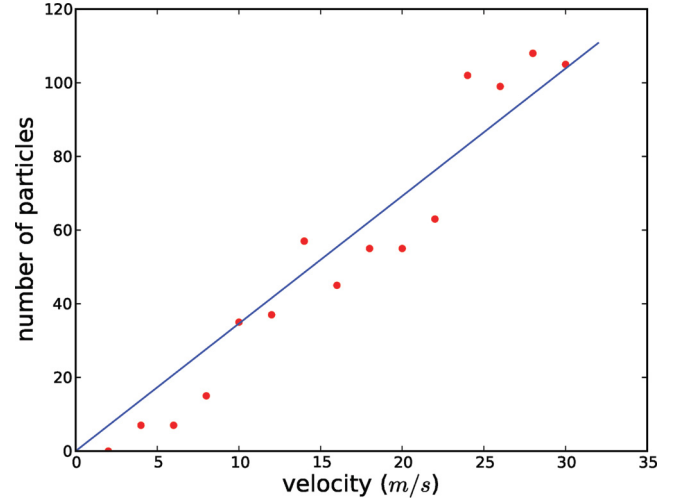


FIG. 9. (Color online) Ejection yield as a function of projectile velocity for a target with filling factor  $\phi = 26.7\%$ .

$\sim 3.7 \times 10^7 \text{ K}$ ; furthermore, our ejection data show a strong tail of grains emitted at high energies (up to  $43.2 \times 10^{-15} \text{ J}$ ), which the exponential decay featured by the Maxwellian distribution cannot describe. We therefore attempt a fit to the so-called Thompson distribution, which characterizes particle ejection in sputtering induced by atom impact [44,45]:

$$f(E) = c \frac{E}{(E + U)^3}. \quad (13)$$

Here,  $c$  is a constant proportional to the total ejection yield, while  $U$  describes the surface binding energy. We note that our simulation data show an apparently even softer decay towards high emission energies than predicted by the  $1/E^2$  falloff of the Thompson law.

In sputtering from solids,  $U$  is well approximated by the cohesive energy of the material. The question arises as to which materials constant our fit value  $U = 1.4 \times 10^{-15} \text{ J}$  corresponds. In granular materials, we may compare to two quantities: (i) the fragmentation energy ( $E_{\text{break}} \sim 2.8 \times 10^{-17} \text{ J}$ ) [Eq. (6)], which is needed to break the contact between two grains; (ii) the so-called rolling energy, i.e., the energy needed to roll two spheres through  $90^\circ$ , and which amounts to  $E_{\text{roll}} \sim 1 \times 10^{-16} \text{ J}$ . We conclude that the fit value of  $U$  is more than an order of magnitude larger than either of these materials quantities. On average, a grain needs to break around 50 contacts with surrounding grains, or alternatively, around 15 roll events, before it is ejected.

Grains are emitted from depths up to  $8R_{\text{grain}}$ ; note that the projectile penetrates down to  $(45.5 \pm 2)R_{\text{grain}}$ . However, the majority of grains originate from around  $(1 - 4)R_{\text{grain}}$ . Such a broad distribution demonstrates that emission occurs throughout the penetration process. While the projectile digs its way down into the target, it imparts momentum to the grains that it shuffles aside. This momentum is mainly directed in the direction down into the target (leading to the compaction described in Sec. III C above) and sideways. However, due to collisions with other grains, the momentum of the colliding grains (or of other recoiling grains) can be redirected such that eventually emission is possible. This mechanism is reminiscent

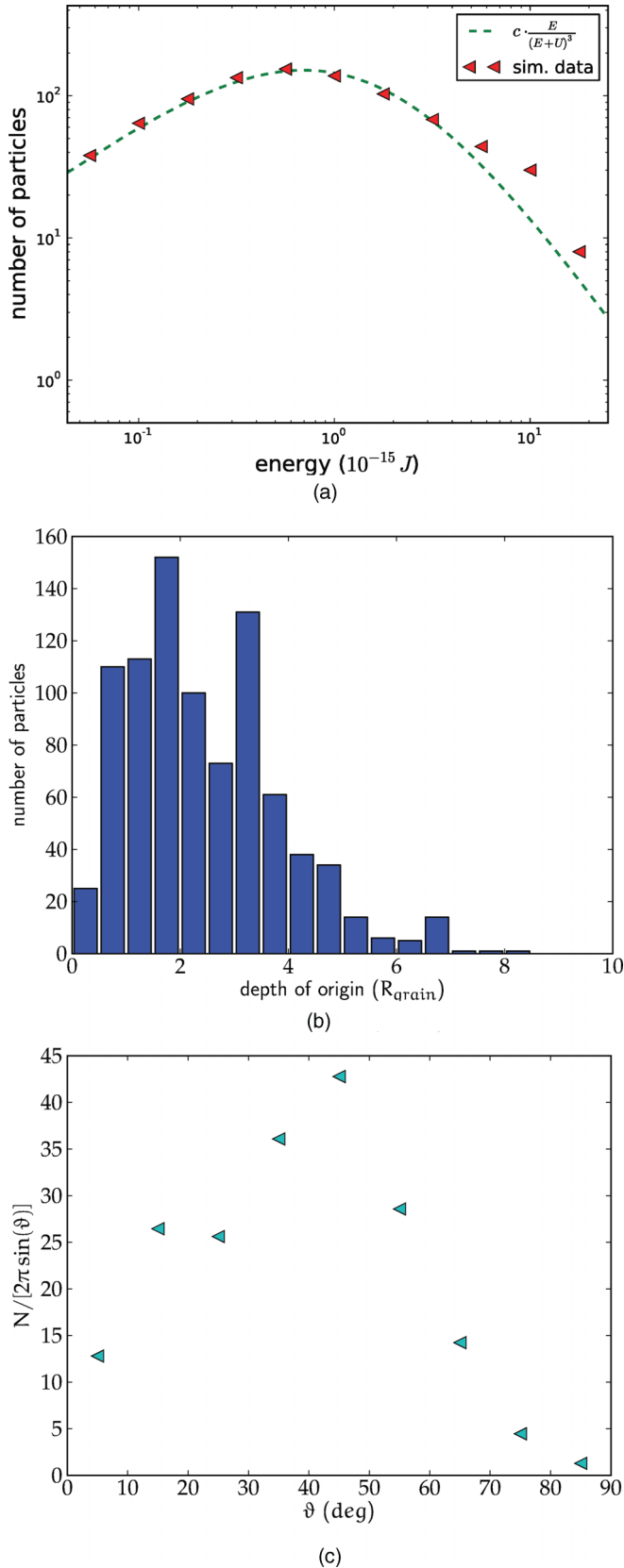


FIG. 10. (Color online) Characteristics of grain ejection caused by impact onto a target with filling factor  $\phi = 26.7\%$  with velocity of 30 m/s. Distribution of (a) ejection energies, (b) depth of origin, and (c) ejection angles, measured with respect to the surface normal. In (a), a Thompson distribution, Eq. (13), is included as a reference.

of the collision-cascade mechanism well known in the theory of sputtering of solids bombarded by energetic ions [45].

We note that also clusters are emitted. Around 32% of all emitted grains have been ejected in the form of clusters, the majority of them (15%) as dimers and 5.4% as trimers. The cluster mass distribution then decreases, and the largest emitted cluster we observed consisted of ten grains.

For the presentation of the angular distribution of ejecta  $N(\vartheta)$ , we divide by the pertinent spherical area and plot

$$N(\vartheta)/(2\pi \sin \vartheta) \quad (14)$$

in Fig. 10(c). We see that emission is far from isotropic; emission along oblique angles,  $\vartheta \sim 45^\circ$ , is strongly preferred. While isotropic emission would be compatible with emission from a flat undisturbed surface, emission from a deep crater would enhance ejection angles close to the surface normal, around  $\vartheta = 0^\circ$ . The oblique emission observed here must hence be due to the emission in the small cone opening between the downward-moving projectile and the crater walls.

#### IV. CONCLUSIONS

Using a granular-mechanics code, we study the impact of a rigid sphere into a porous adhesive granular target, consisting of monodisperse silica grains. The model includes elastic repulsive, adhesive, and dissipative forces, as well as sliding, rolling, and twisting friction. Impact velocities up to 30 m/s, and target filling factors (densities) between 19% and 35%, have been systematically studied. We find:

(1) The projectile is stopped by an effective drag force which is proportional to the square of its velocity, as predicted by some models like the so-called Poncelet law, and observed in several experiments.

(2) The penetration depth depends approximately logarithmically on the impact velocity and is inversely proportional to the target density.

(3) Target adhesion influences projectile stopping only below a critical velocity, which increases with adhesion  $\gamma$ . The grains in front of the projectile form an adhesive stopping cushion, which stops the projectile efficiently due to its large effective mass.

(4) The excavated crater is of conical form and is surrounded by a compaction zone, whose width increases, but whose maximum value decreases with increasing target density. Such conical craters display some similarities with craters formed at much higher impact velocities in the STARDUST mission aerogel collector.

(5) Grain ejection increases in proportion with impactor velocity.

(6) Grains are ejected which have originally been buried up to a depth of  $8R_{\text{grain}}$  below the surface; their angular distribution favors oblique ejection with a maximum around  $45^\circ$ . The velocity distribution of ejected grains features a broad low-velocity maximum around 0.5 – 1 m/s, but exhibits a high-velocity tail up to  $\sim 15\%$  of the projectile impact velocity.

Future simulations with projectiles having internal structure would allow projectile fragmentation, and therefore the formation of more complex crater shapes, possibly including a thin track extending from the bottom of the main crater.

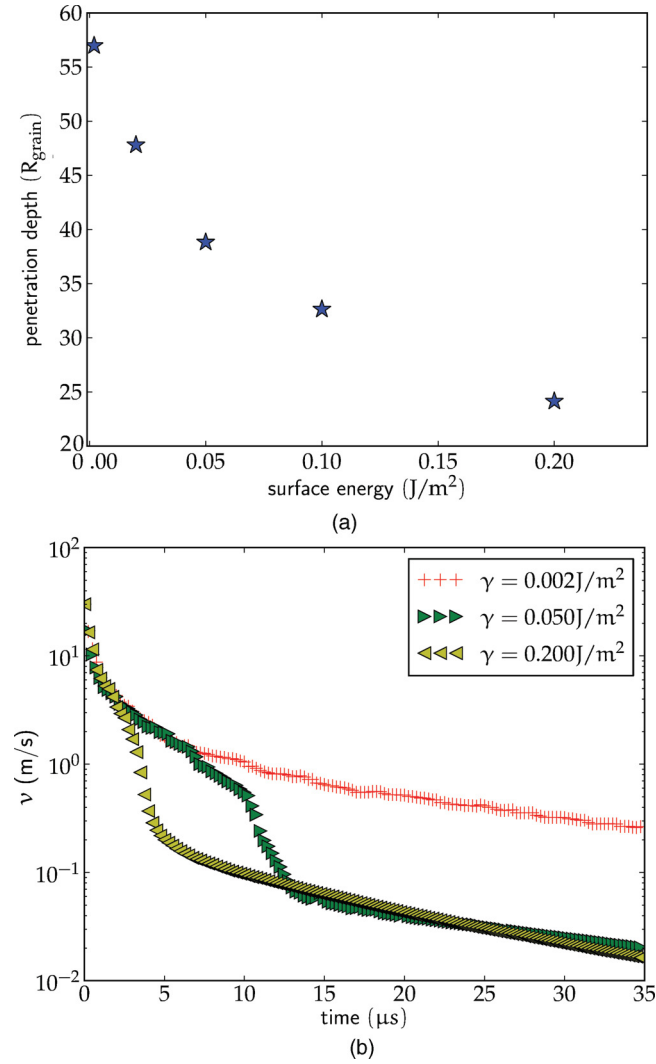


FIG. 11. (Color online) Influence of the surface energy of grains  $\gamma$  on (a) the penetration depth and (b) the slowing down of the projectile. Data are for projectile impact at 30 m/s into a target with filling factor of 30.7%.

#### ACKNOWLEDGMENTS

This work has been supported by the *Deutsche Forschungsgemeinschaft* via the Graduiertenkolleg 814. E.M.B. acknowledges support from CONICET, SeCTyP (U.N. Cuyo), and PICT-2009-0092.

#### APPENDIX: INFLUENCE OF SURFACE ENERGY

We investigate in this Appendix how the value of the surface energy  $\gamma$  influences the stopping and penetration of the projectile. To this end we performed simulations in which  $\gamma$  was varied between 2 and 200  $\text{mJ/m}^2$  around the nominal value of 50  $\text{mJ/m}^2$ , for which this model was set up. In this study, the projectile always impacts with a velocity of 30 m/s into a target with filling factor of 30.7%.

We note that according to Sec. II A,  $\gamma$  influences the dynamics in two respects since (i) the adhesion force [Eq. (2)] and (ii) the rolling friction [Eq. (4)] are proportional to  $\gamma$ .

We observe in Fig. 11(a) that projectile penetration decreases monotonically with  $\gamma$ . The penetration depth  $D = 57R_{\text{grain}}$  for our smallest value of  $\gamma$ , 2  $\text{mJ/m}^2$ , will be identical to the penetration in a nonadhesive powder. It is almost 50% larger than the penetration in adhesive silica dust with the realistic value of  $\gamma = 50 \text{ mJ/m}^2$ . A further fourfold increase of  $\gamma$  to 200  $\text{mJ/m}^2$  reduces the penetration by 40% to  $D = 24R_{\text{grain}}$ .

In order to gain more insight into the influence of adhesion on the stopping process, we plot in Fig. 11(b) the temporal evolution of the projectile velocity. The velocities for the standard case,  $\gamma = 50 \text{ mJ/m}^2$ , coincide for the first 7  $\mu\text{s}$  with those plotted in Fig. 2; they correspond to stopping according to the Poncelet force law [Eq. (8)] with  $\alpha = 2$ :  $F \propto v^2$ . We verified that the velocity for the smallest adhesion,  $\gamma = 2 \text{ mJ/m}^2$ , follows Eq. (9) throughout the first 35  $\mu\text{s}$  plotted in Fig. 11(b).

Figure 11(b) thus gives us the following picture. Initially, target adhesion is irrelevant for projectile stopping. In this *ballistic* phase, stopping follows Poncelet's law as discussed in Refs. [7] and [6]. With decreasing projectile velocity, target adhesion becomes important and leads to a strong increase of the stopping force; the critical velocity below which adhesion becomes important increases with increasing  $\gamma$ . We are not aware of a theoretical analysis of the *adhesion-increased stopping* force. The physical picture behind it is that the projectile no longer interacts with individual target grains but with an agglomerate (a stopping *cushion*) of target grains held together by adhesion; due to its increased mass, it can stop the projectile more efficiently.

Finally, after the projectile velocity has decreased to values of  $\sim 0.1 \text{ m/s}$ , the stopping force becomes smaller again. This is a consequence of the viscous force law entering the friction forces for small velocities (see our discussion at the end of Sec. II A). However, at this time the projectile velocity is already so small that penetration is only marginally affected by this third stopping stage.

We note that we saw an analogous behavior if we vary the target density for constant adhesion. In this case the Poncelet law holds for larger times in thinner targets. This is plausible since *adhesion-increased stopping* works via the buildup of a temporary target cushion which will be less effective in thin targets.

We summarize our findings on the influence of adhesion on stopping as follows. At large velocities, the projectile is stopped ballistically, as in Poncelet's law. Below a critical velocity, which increases with adhesion  $\gamma$ , the projectile is stopped considerably more strongly. The reason hereto lies in the formation of an adhesive target cushion in front of the projectile, which stops the projectile efficiently due to its large effective mass.

[1] J. S. Uehara, M. A. Ambroso, R. P. Ojha, and D. J. Durian, *Phys. Rev. Lett.* **90**, 194301 (2003); **91**, 149902(E) (2003).

[2] A. M. Walsh, K. E. Holloway, P. Habdas, and J. R. de Bruyn, *Phys. Rev. Lett.* **91**, 104301 (2003).

- [3] D. Lohse, R. Bergmann, R. Mikkelsen, C. Zeilstra, D. van der Meer, M. Versluis, K. van der Weele, M. van der Hoef, and H. Kuipers, *Phys. Rev. Lett.* **93**, 198003 (2004).
- [4] M. Pica Ciamarra, A. H. Lara, A. T. Lee, D. I. Goldman, I. Vishik, and H. L. Swinney, *Phys. Rev. Lett.* **92**, 194301 (2004).
- [5] M. Hou, Z. Peng, R. Liu, K. Lu, and C. K. Chan, *Phys. Rev. E* **72**, 062301 (2005).
- [6] L. S. Tsimring and D. Volfson, in *Powders and Grains 2005*, edited by R. Garcia-Rojo, H. J. Herrmann, and S. McNamara (A. A. Balkema, Rotterdam, 2005), p. 1215.
- [7] H. Katsuragi and D. J. Durian, *Nat. Phys.* **3**, 420 (2007).
- [8] H. Katsuragi, *Phys. Rev. Lett.* **104**, 218001 (2010).
- [9] J. R. C. Garry, M. C. Towner, A. J. Ball, J. C. Zarnecki, and G. Marcou, *Adv. Space Res.* **23**, 1229 (1999).
- [10] M. F. A'Hearn, M. J. S. Belton, W. A. Delamere, J. Kissel, K. P. Klaasen, L. A. McFadden, K. J. Meech, H. J. Melosh, P. H. Schultz, J. M. Sunshine *et al.*, *Science* **310**, 258 (2005).
- [11] R. A. Kerr, *Science* **309**, 1667 (2005).
- [12] F. Hörz, R. Bastien, J. Borg, J. P. Bradley, J. C. Bridges, D. E. Brownlee, M. J. Burchell, M. Chi, M. J. Cintala, Z. R. Dai *et al.*, *Science* **314**, 1716 (2006).
- [13] Y. Iida, A. Tsuchiyama, T. Kadono, K. Sakamoto, T. Nakamura, K. Uesugi, T. Nakano, and M. E. Zolensky, *Meteorit. Planet. Sci.* **45**, 1302 (2010).
- [14] G. Dominguez, *Meteorit. Planet. Sci.* **44**, 1431 (2009).
- [15] J. R. Royer, D. J. Evans, L. Oyarte, Q. Guo, E. Kapit, M. E. Möbius, S. R. Waitukaitis, and H. M. Jaeger, *Nature (London)* **459**, 1110 (2009).
- [16] J. R. Royer, E. I. Corwin, P. J. Eng, and H. M. Jaeger, *Phys. Rev. Lett.* **99**, 038003 (2007).
- [17] G. Caballero, R. Bergmann, D. van der Meer, A. Prosperetti, and D. Lohse, *Phys. Rev. Lett.* **99**, 018001 (2007).
- [18] D. Paszun and C. Dominik, *Astron. Astrophys.* **507**, 1023 (2009).
- [19] K. Wada, H. Tanaka, T. Suyama, H. Kimura, and T. Yamamoto, *Astrophys. J.* **661**, 320 (2007).
- [20] K. Wada, H. Tanaka, T. Suyama, H. Kimura, and T. Yamamoto, *Astrophys. J.* **677**, 1296 (2008).
- [21] T. Suyama, K. Wada, and H. Tanaka, *Astrophys. J.* **684**, 1310 (2008).
- [22] K. Wada, H. Tanaka, T. Suyama, H. Kimura, and T. Yamamoto, *Astrophys. J.* **702**, 1490 (2009).
- [23] K. Wada, H. Tanaka, T. Suyama, H. Kimura, and T. Yamamoto, *Astrophys. J.* **737**, 36 (2011).
- [24] M. Jutzi and E. Asphaug, *Nature (London)* **476**, 69 (2011).
- [25] M. Jutzi, W. Benz, and P. Michel, *Icarus* **198**, 242 (2008).
- [26] M. Jutzi, P. Michel, K. Hiraoka, A. M. Nakamura, and W. Benz, *Icarus* **201**, 802 (2009).
- [27] R. J. Geretshauser, F. Meru, R. Speith, and W. Kley, *Astron. Astrophys.* **531**, A166 (2011).
- [28] C. Ringl and H. M. Urbassek, *Comput. Phys. Commun.* **183**, 986 (2012).
- [29] C. Ringl, E. M. Bringa, D. S. Bertoldi, and H. M. Urbassek, *Astrophys. J.* **752**, 151 (2012).
- [30] T. Pöschel and T. Schwager, *Computational Granular Dynamics: Models and Algorithms* (Springer, New York, 2005).
- [31] N. V. Brilliantov, F. Spahn, J.-M. Hertzsch, and T. Pöschel, *Phys. Rev. E* **53**, 5382 (1996).
- [32] B. V. Derjaguin, V. M. Muller, and Y. P. Toporov, *J. Colloid Interface Sci.* **53**, 314 (1975).
- [33] K. L. Johnson, K. Kendall, and A. D. Roberts, *Proc. R. Soc. London A* **324**, 301 (1971).
- [34] K. L. Johnson, *Contact Mechanics* (Cambridge University Press, Cambridge, 1985).
- [35] D. Maugis, *Contact, Adhesion and Rupture of Elastic Solids* (Springer, Berlin, 2000).
- [36] I. Szlufarska, M. Chandross, and R. W. Carpick, *J. Phys. D* **41**, 123001 (2008).
- [37] N. Burnham and A. A. Kulik, in *Handbook of Micro/Nano Tribology*, 2nd ed., edited by B. Bhushan (CRC Press, Boca Raton, FL, 1999), Chap. 5, p. 247.
- [38] C. Dominik and A. G. G. M. Tielens, *Astrophys. J.* **480**, 647 (1997).
- [39] <http://lammmps.sandia.gov/>.
- [40] A. Chokshi, A. G. G. M. Tielens, and D. Hollenbach, *Astrophys. J.* **407**, 806 (1993).
- [41] J. Blum and R. Schräpler, *Phys. Rev. Lett.* **93**, 115503 (2004).
- [42] M. E. Backman and W. Goldsmith, *Int. J. Eng. Sci.* **16**, 1 (1978).
- [43] *Sputtering by Particle Bombardment*, edited by R. Behrisch (Springer, Berlin, 1981), Vol. 1; (Springer, Berlin, 1983), Vol. 2; (Springer, Berlin, 1991), Vol. 3.
- [44] M. W. Thompson, *Philos. Mag.* **18**, 377 (1968).
- [45] P. Sigmund, in *Sputtering by Particle Bombardment I*, edited by R. Behrisch (Springer, Berlin, 1981), p. 9.